# A Novel Low-Pressure Robotic Glove Based on CT-Optimized Finger Joint Kinematic Model for Long-Term Rehabilitation of Stroke Patients

Jinxu Yu, Lei Luo, Wenzhao Zhu, Yongquan Li, Ping Xie, and Lijie Zhang

***Abstract*— Wearing robotic gloves has become increasingly crucial for hand rehabilitation in stroke patients. However, traditional robotic gloves can exert additional pressure on the hand, such as prolonged use leading to poor blood circulation and muscle stiffness. To address these concerns, this work analyzes the finger kinematic model based on computerized tomography (CT) images of human hands, and designs a low-pressure robotic glove that conforms to finger kinematic characteristics. Firstly, physiological data on finger joint flexion and extension were collected through CT scans. The equivalent rotation centers of finger joints were obtained using the SURF and RANSAC algorithms. Furthermore, the trajectory of finger joint end and the correlation equation of finger joint motion were fitted, and a comprehensive finger kinematic model was established. Based on this finger kinematic model, a novel under-actuated exoskeleton mechanism was designed using a human-machine integration approach. The novel robotic glove fully aligns with the equivalent rotation centers and natural motion trajectories of the fingers, exerting minimal and evenly distributed dynamic pressure on the fingers, with a theoretical static pressure value of zero. Experiments involving gripping everyday objects demonstrated that the novel robotic glove significantly reduces the overall pressure on the fingers during grasping compared to the pneumatic glove and the traditional exoskeleton robotic glove. It is suitable for long-term use by stroke patients for rehabilitation training.**

***Index Terms*— Robotic glove, computed tomography (CT) analysis, under-actuated exoskeleton, low pressure.**

Manuscript received 22 August 2023; revised 20 November 2023; accepted 24 November 2023. Date of publication 30 November 2023; date of current version 12 January 2024. This work was supported in part by the National Natural Science Foundation of China under Grant U20A20192, in part by the Natural Science Foundation of Hebei Province of China under Grant F2022203079, and in part by the Key Research and Development Program of Hebei Province of China under Grant 21372005D. *(Corresponding author: Lijie Zhang.)*

This work involved human subjects or animals in its research. Approval of all ethical and experimental procedures and protocols was granted by the Ethics Committee of Qinhuangdao First Hospital under Approval No. 2023G010-2.

Jinxu Yu is with the School of Mechanical Engineering, Yanshan University, Qinhuangdao 066004, China (e-mail: yujinxu@stumail.ysu.edu.cn).

Lei Luo is with the Key Laboratory of Optoelectronic Technology and Systems, Education Ministry of China, Chongqing University, Chongqing 400044, China (e-mail: llei@cqu.edu.cn).

Wenzhao Zhu and Ping Xie are with the Key Laboratory of Intelligent Control and Neural Information Processing, Education Ministry of China, Yanshan University, Qinhuangdao 066004, China (e-mail: wenzhaozhu@ysu.edu.cn; pingx@ysu.edu.cn).

Yongquan Li and Lijie Zhang are with the Key Laboratory of Advanced Forging Stamping Technology and Science, Education Ministry of China, Yanshan University, Qinhuangdao 066004, China (e-mail: lijiang197879@sina.com; ljzhang@ysu.edu.cn).

Digital Object Identifier 10.1109/TNSRE.2023.3337827

## I. Introduction

WEARABLE robotic gloves have emerged as a primary choice for hand rehabilitation among stroke patients [1], [2], [3], [4], [5]. These gloves offer patients the benefit of repetitive and continuous rehabilitation therapy. Patients can utilize these robotic gloves to assist them in daily activities, facilitating ongoing rehabilitation exercises [6]. This continuous therapy contributes to enhanced hand muscle mobility, improved neural connectivity, and the development of finer finger dexterity and coordination [7], [8], [9]. However, prolonged use of robotic gloves can exert pressure on the hand, resulting in issues like reduced blood circulation and muscle stiffness. This pressure stems from various sources, including static, dynamic, and antagonistic pressures generated by the robotic glove itself [10]. The glove carries a certain weight and must fit snugly to prevent any dislocation, leading to static pressure on the fingers. Additionally, the robotic glove's exertion of force to assist finger flexion and extension creates dynamic pressure. Furthermore, if the glove's structure does not align well with the natural finger movement trajectory during flexion and extension, it can create conflicting forces, leading to additional antagonistic pressure. Consequently, these combined pressures generated by the robotic glove can result in discomfort or pain during extended rehabilitation periods and increase the risk of skin damage [11]. Hence, there is a pressing need for the development of a robotic glove designed to minimize hand pressure, enhance comfort, and enable extended wear.

The pressure exerted on the hand by a robotic glove is contingent upon its compatibility with the finger's physiological structure. Therefore, a pivotal aspect in the design of a low-pressure and comfortable robotic glove lies in understanding the finger's physiological structure and motion characteristics. Studies have progressed from initial observations of joint angles using 2-D images [12] to more comprehensive multi-joint motion analyses through 3-D videos [13], [14]. Subsequently, wearable multi-angle sensors [15] and motion capture systems [16], [17] have been employed to determine the angular correlations among individual joints and the motion trajectory of the finger's tip. However, it's worth noting that the aforementioned research did not account for the position of the finger joint's center of rotation (COR). Neglecting this aspect could potentially result in misalignment between the COR of the robotic glove joint and that of the finger joint. Utilizing CT technology and analyzing CT images of the phalanx [18], [19], [20], [21], [22], [23], researchers have gradually elucidated the contact mode of the phalanx at the joint [18], [24], [25], [26]. This investigation has revealed a translation phenomenon in the phalanx, further substantiating that the knuckles do not rotate at a fixed center but rather exhibit dynamic changes with the flexion and extension of the fingers [27], [28]. Intriguingly, this distinctive kinematic characteristic of the knuckles has yet to be integrated into the current robotic glove design process.

The design of an exoskeleton structure for a robotic glove must closely align with the kinematic characteristics of the finger joints. Otherwise, the exoskeleton structure will fail to replicate natural finger movements, resulting in significant antagonistic pressure. Before embarking on the design of the exoskeleton structure, Robson and Soh [9] introduced a straightforward kinematic chain referred to as the "anthropometric back-bone chain." The entire configuration of the exoskeleton is based on this kinematic chain. While the motion of the anthropometric back-bone chain closely approximates the physiological motion of the fingers, it falls short in ensuring that the COR of the fingers coincides with it. This limitation arises because the anthropometric back-bone chain is fundamentally a three-link kinematic chain with the fixed COR. To address this issue, Jo et al. [29] employed motion capture equipment to gather data on joint rotations and motion trajectories during finger flexion and extension. They established correlation equations for the metacarpophalangeal (MCP) and proximal interphalangeal (PIP) joints and determined the lengths of the finger's proximal, middle, and distal segments in a 5:3:2 ratio based on external observations. This approach led to a relatively comprehensive but imprecise kinematic model of finger joints. However, even in this model, the dynamic changes in the positions of the CORs of each joint during motion were not considered.

Based on all mentioned above, there are two main limitations in reducing pressure on the fingers and improving the comfort of wearing robotic gloves: (1) Traditional work primarily relies on observing kinematic data of the hand through CT images, lacking the analysis to extract key kinematic features of finger joints. As a result, it becomes impossible to establish a finger joint kinematic model that can be integrated with the design of finger exoskeleton structures [30], [31], [32]. (2) In the process of designing the exoskeleton structure, there is insufficient consideration of the kinematic characteristics of finger joints. This oversight leads to deviations between the motion trajectory of the exoskeleton and the natural physiological trajectory of the fingers, resulting in higher antagonistic pressure, reduced comfort, and the potential for injuries with prolonged use [33], [34].

To tackle these issues, a novel low-pressure robotic glove based on a CT-optimized kinematic model of the finger joints is proposed. The primary innovations can be summarized as follows: (1) Utilizing CT image processing, we have acquired the COR points for each joint throughout the entire range of finger movements. By analyzing the positions of these COR points, we calculate a representative equivalent rotation center. Subsequently, leveraging this equivalent rotation center and CT image data, we have developed time-sequence functions for joint angles and angular velocities. This has allowed us to establish trajectory equations for the movement of the joint's end and correlation equations describing joint motion. (2) Leveraging the finger kinematics model and an under-actuated exoskeleton structure, and with the aid of configuration transformations and joint motion correlation equations, we have successfully formulated solvable constraint equations for the under-actuated configuration. Furthermore, thanks to the relatively precise finger joint kinematics model, the novel exoskeleton structure theoretically imposes no antagonistic pressure. This innovation translates into a reduction in overall pressure on the fingers, significantly enhancing wearing comfort.

The remainder of the paper is structured as follows: In Section II, we present the finger motion features obtained from CT data and establish a comprehensive finger kinematic model. Section III provides a detailed illustration of the novel under-actuated exoskeleton structure. To validate the effectiveness of our proposed method, we conduct numerical simulations and experiments in Section IV. Lastly, in Section V, we draw conclusions based on our works.

## II. Establishing Finger Kinematic Model Based on Computed Tomography (CT) Image Analysis

### A. CT Image Acquisition and Preprocessing

CT imaging offers the most effective means of observing the index finger and the interaction between adjacent phalanges [26]. The number of CT scans subjects receive needs to be within safe limits due to radiation. According to the calculation basis provided in the literature [35] and [36], combined with the scanning site and CT equipment in this experiment, each subject was allowed 10 CT image acquisitions of the index finger those subjects who had not had a CT scan in the past year. For further safety considerations, only 5 index finger CT scans were scheduled for each subject. The CT experimental setup is depicted in Fig. 1. To investigate more precise finger motion features, a complete set of finger flexion-extension movements was divided into 10 poses at equal time intervals, as shown in Fig. 2. Since each subject could only undergo finger CT scanning for 5 poses, it required two subjects with similar finger characteristics to complete a full set of finger flexion-extension motion CT scans. We recruited 50 healthy participants, comprising 34 males and 16 females. The participants' ages were concentrated between 20 and 27 years old, with weights ranging from 57 to 69 kg, and heights spanning 167 to 179 cm. None of the participants had a history of hand injuries or other pathological conditions and had not received a CT scan within the last year. When dividing the subject groups, we sorted all the subjects based on the length of their index fingers and grouped individuals with the most similar finger characteristics into a single group. This resulted in a

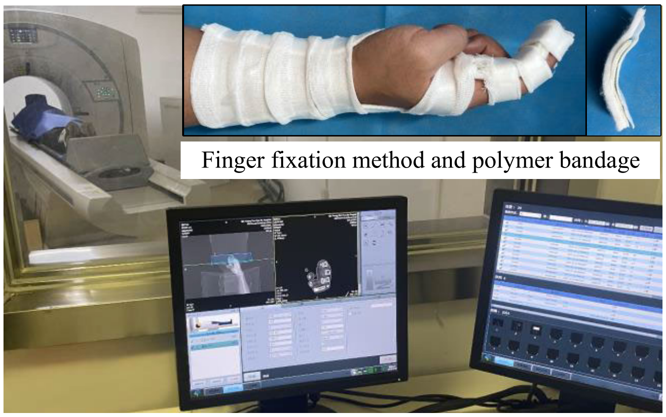


Fig. 1. CT environment and the fixation method in the experiment.

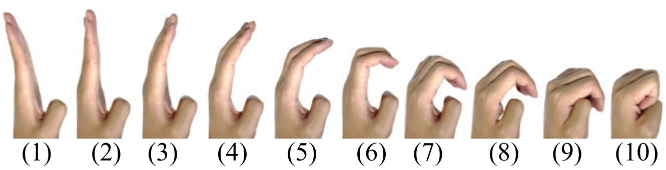


Fig. 2. Ten finger postures for CT experiment.

total of 25 groups, each consisting of 2 individuals. The CT image data collection mentioned in this article has received approval from the Ethics Committee of The First Hospital of Qinhuangdao City. The approval number is 2023G010-2, and the approval date is March 15, 2023.

After completing the CT image acquisition for each group of subjects, it was necessary to perform CT image preprocessing to obtain valid finger bone posture data. In the initial stages, we employ methods such as thresholding, region growing, and mask establishment to distinguish the bones from the surrounding soft tissues and skin [37]. Following this, thresholding segmentation is utilized to partition the entire hand skeleton into metacarpals, proximal phalanges, middle phalanges, and distal phalanges. Lastly, we create a central skeletal slice to convert the three-dimensional skeletal point cloud data into two-dimensional image data [18]. The resulting CT images after preprocessing are depicted in Fig. 3.

### B. Extraction of Rotation Center Points and Equivalent Rotation Center

Once we have acquired central cross-sectional images of the index finger in all 10 postures, the next step is to compare the positions of the finger bones in the images of adjacent postures. This comparative analysis enables us to pinpoint the CORs of the finger bones during the transitional movement between these two postures [27]. To determine the COR of the proximal phalanx, we first align the head of the palm bone in all 10 postures within a unified coordinate system. This alignment process facilitates the calculation of precise coordinates for the COR of the proximal phalanx as it pivots around the palm bone. Similarly, we can calculate the specific coordinates of the CORs for the middle and distal phalanges as they pivot around the preceding finger bone.

When dealing with adjacent phalangeal CT images registered within a unified coordinate system, we employ the

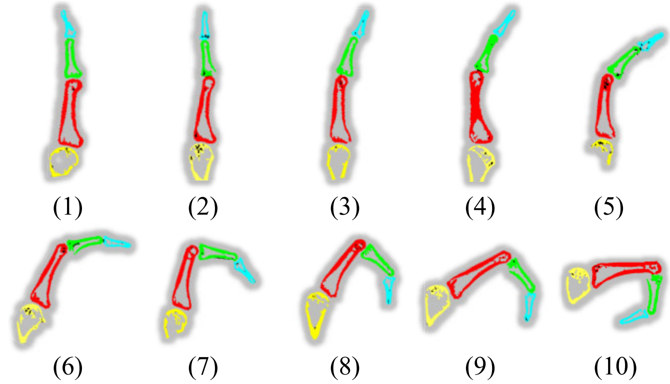


Fig. 3. Central cross-sectional images of the index finger.

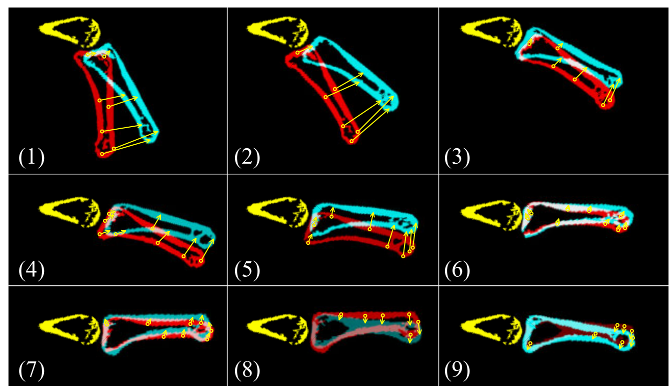


Fig. 4. Extraction process of center of rotation(COR).

Speeded-Up Robust Features (SURF) algorithm [38] for key point extraction and feature description. The SURF algorithm excels at identifying key points within the image, considering each key point as a center and utilizing image gradient information to compute feature descriptors for the region surrounding the key point at a specific scale.

After acquiring the key point descriptors, the key points from two adjacent frames of phalanx images are matched. Subsequently, the correct matching pairs are identified and filtered using the Random Sample Consensus (RANSAC) algorithm [39]. The final matching model, and the paired description of the adjacent frame phalanx images is shown in Fig. 4.

Finally, the transformation matrix of the finger bones in different poses acquired by RANSAC algorithm is given as:

$$T = \begin{bmatrix} \cos(\theta) & -\sin(\theta) & t_x \\ \sin(\theta) & \cos(\theta) & t_y \\ 0 & 0 & 1 \end{bmatrix}, \quad (1)$$

where, $\theta$ represents the rotation angle, and $(t_x, t_y)$ represents the translation vector. The fundamental principle for estimating the COR is to minimize the distance between the transformed point and the original point. This can be accomplished by minimizing the sum of squared residuals, as expressed by the equation:

$$\text{minimize} \sum_i \Big\{ (\cos(\theta) \cdot x_i - \sin(\theta) \cdot y_i - x_i')^2 + (\sin(\theta) \cdot x_i + \cos(\theta) \cdot y_i - y_i')^2 \Big\}, \quad (2)$$

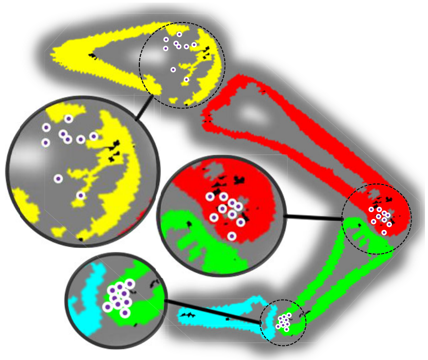

Fig. 5. Visualization of center of rotation (COR).

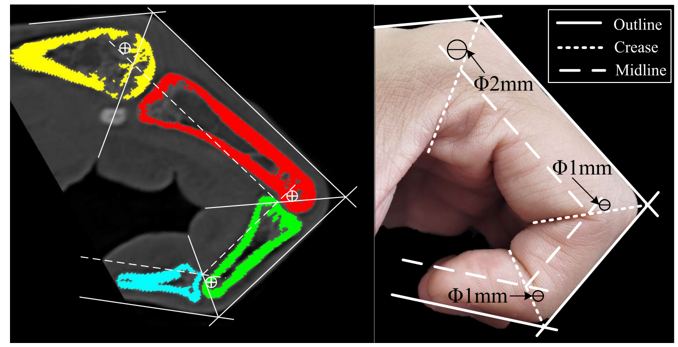


Fig. 6. Equivalent rotation centers of finger.

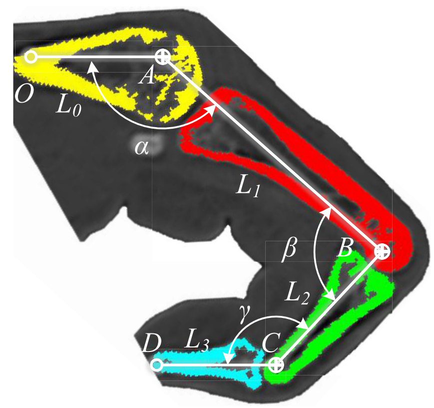


Fig. 7. Finger phalangeal motion model.

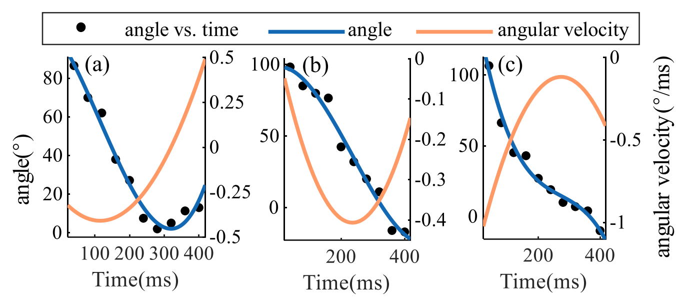


Fig. 8. Time-sequence function curve and joint angular velocity, (a) MCP joint, (b) PIP joint, (c) DIP joint.

where $(x_i, y_i)$ denotes the coordinates of the points in the original image, and $(x_i', y_i')$ denotes the corresponding points coordinates in the transformed image. To minimize the objective function mentioned above, we compute the derivatives with respect to $\theta$ and $(t_x, t_y)$ and set them to zero. Through solving for the obtained rotation angle $\theta$, we can calculate the coordinates of the rotation center, i.e., the position of the rotation center in the original image coordinate system. This process results in the determination of multiple positions of the COR in the original image coordinate system, corresponding to the COR points of each joint. Several COR positions, represented by white circles, are visualized in Fig. 5.

By observing the distribution of the 9 sets of CORs, it is evident that they lack regularity and cannot be directly applied to exoskeleton design. To ensure that the structure of the robotic glove can align with the CORs of the finger joints, it is necessary to determine representative equivalent rotation centers. We calculate the average coordinates of the rotation centers for each joint from the 9 sets of data, as illustrated in Fig. 6(a). However, in practical engineering applications, it is challenging to rely on CT imaging every time to precisely determine the equivalent rotation centers. Through extensive experimentation and validation, we have developed an empirical method for locating equivalent rotation centers that leverages skin creases at the finger joints and the geometric centerline of the finger, as depicted in Fig. 6(b). The process is as follows: (1) Keep the fingers slightly bent and mark the outline, crease line, and midline separately. (2) Create a positioning circle that is tangent to both the crease line and the midline. Position this circle within the acute-angle space formed by the crease line and the midline. (3) Due to the greater dispersion of CORs at the MCP joint, the radius of the positioning circle at the MCP joint is 2mm, while at other joints, it is 1mm. In engineering applications, the positioning accuracy is generally around 1mm. Therefore, any point within the circle can be chosen as the equivalent rotation center. If higher positioning accuracy is required, the center point of the circle is preferred as the equivalent rotation center.

### C. Establishment and Analysis of Finger Kinematic Model

*1) Create the Time-Sequence Function of Joint Rotation:* In the preceding section, we determined the equivalent rotation center for each joint, allowing us to create an initial phalangeal motion model illustrated in Fig. 7. In this model, $L_0$ represents the length of the metacarpophalangeal ($OA$), whereas $L_1$, $L_2$, and $L_3$ represent the lengths of the proximal phalanx ($AB$), the middle phalanx ($BC$), and the distal phalanx ($CD$), respectively. Points $A$, $B$, and $C$ denote the equivalent centers of rotation for the MCP, the PIP, and the distal interphalangeal (DIP) joints, respectively. Additionally, $\alpha$, $\beta$, and $\gamma$ signify the articulation angles at the MCP, PIP, and DIP joints, respectively. Furthermore, Fig. 8 illustrates the fitting time-sequence function curve and joint angular velocity for each joint angle data.

*2) Joint End Trajectory Equation:* Based on the time-sequence function, the trajectory of each joint end is determined. The trajectory of the joint end can be calculated separately as follows:

$$\begin{cases} x_B(t) = L_1 \cdot \cos\alpha(t) \\ y_B(t) = L_1 \cdot \sin\alpha(t), \end{cases} \tag{3}$$

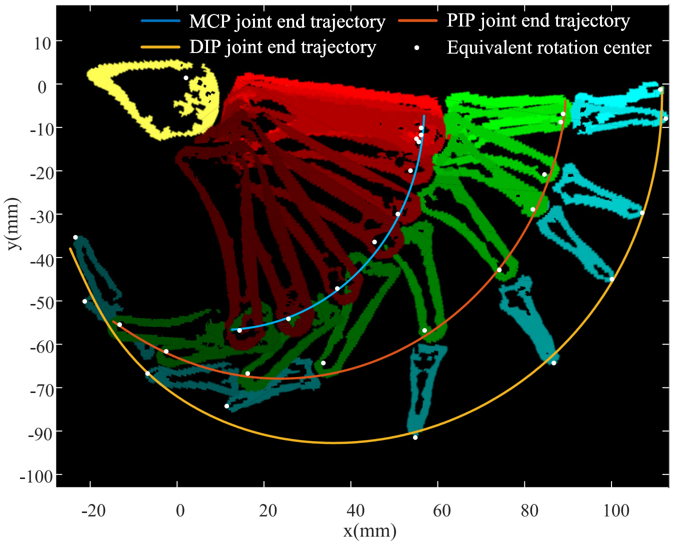


Fig. 9. Trajectory of the index finger joint end and its equivalent rotation center obtained from CT images.

$$\begin{cases} x_C(t) = L_1 \cdot \cos\alpha(t) + L_2 \cdot \cos\beta(t) \\ y_C(t) = L_1 \cdot \sin\alpha(t) + L_2 \cdot \sin\beta(t), \end{cases} \tag{4}$$

$$\begin{cases} x_D(t) = L_1 \cdot \cos\alpha(t) + L_2 \cdot \cos\beta(t) + L_3 \cdot \cos\gamma(t) \\ y_D(t) = L_1 \cdot \sin\alpha(t) + L_2 \cdot \sin\beta(t) + L_3 \cdot \sin\gamma(t). \end{cases} \tag{5}$$

The comparison between the joint end trajectory and the end trajectory points in CT images, as shown in Fig. 9, reveals that the joint endpoint trajectory obtained from the joint time-sequence functions can effectively simulate the actual variations in joint end trajectories.

*3) Finger Joint Motion Correlation:* The purpose of establishing a finger kinematic model is to integrate it into exoskeleton design, aiming to enhance human-machine compatibility and reduce the pressure exerted by the exoskeleton on the hand. However, due to the absence of temporal information in the exoskeleton's constraint equations, the joint angle time-sequence functions and end trajectory equations cannot be directly utilized. Therefore, we established an angle mapping between $\alpha$, $\beta$, and $\gamma$, as shown in Fig.10. The equation describing the correlation of finger joint motion, obtained through data fitting, is as follows:

$$\alpha(\beta) = 0.1087\beta^2 - 18.01\beta + 812.8 \tag{6}$$

$$\gamma(\beta) = 0.3954\beta^2 - 69.21\beta + 3099 \tag{7}$$

where the root mean square error (RMSE) for $\alpha(\beta)$ is 0.04605, and the RMSE for $\gamma(\beta)$ is 0.174, indicating a good fit. Based on this model and function, we have applied a methodology that adds two connecting rods to the base exoskeleton structure for configuration synthesis using adjacency matrices and topological configurations, which is based on our previous research [40]. The final synthesized configuration is shown in Fig. 11, with link $f$ as the frame and $l_1$, $l_2$, $l_5$ and $l_7$ having three hinge points. The segment between the first hinge point and the second hinge point is denoted as $l_{x-1}$, while the rest is referred to as $l_{x-2}$. Both $loop_1$ and $loop_3$ are five-bar linkages, whereas

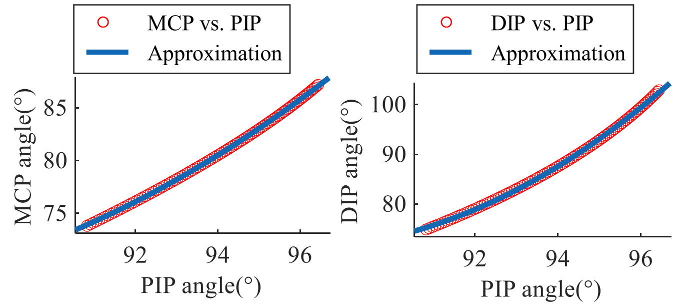


Fig. 10. Fitting of finger joint correlations.

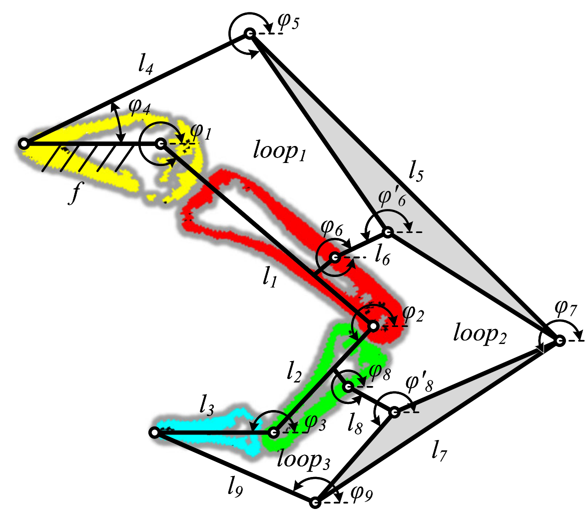


Fig. 11. Structure of the proposed under-actuated exoskeleton.

$loop_2$ is a six-bar linkage. The Lagrangian coordinate system is established with the horizontal right direction as the positive $x$-axis, and counterclockwise angles from the link to the $x$-axis as positive angles. This structure comprises eleven Lagrangian coordinates, namely $\varphi_1$ to $\varphi_9$, $\varphi_6'$, and $\varphi_8'$. Specifically, $\varphi_6'$ and $\varphi_8'$ are related to $\varphi_6$ and $\varphi_8$ as follows:

$$\varphi_6' = \pi + \varphi_6, \varphi_8' = \pi + \varphi_8. \tag{8}$$

There are still nine linearly independent Lagrangian coordinates. Based on the three loops shown in Fig. 11, we can establish the following six constraint equations:

$$\begin{cases} l_{1-1}\cos\varphi_1 + l_4\cos\varphi_4 + l_{5-1}\cos\varphi_5 \\ \quad + l_6\cos(\pi + \varphi_6) - f = 0 \\ l_{1-2}\cos\varphi_1 + l_{2-1}\cos\varphi_2 + l_{5-2}\cos\varphi_5 \\ \quad + l_6\cos\varphi_6 + l_{7-1}\cos\varphi_7 + l_8\cos(\pi + \varphi_8) = 0 \\ l_{2-2}\cos\varphi_2 + l_3\cos\varphi_3 + l_{7-2}\cos\varphi_7 \\ \quad + l_8\cos\varphi_8 + l_9\cos\varphi_9 = 0 \\ l_{1-1}\sin\varphi_1 + l_4\sin\varphi_4 + l_{5-1}\sin\varphi_5 \\ \quad + l_6\sin(\pi + \varphi_6) = 0 \\ l_{1-2}\sin\varphi_1 + l_{2-1}\sin\varphi_2 + l_{5-2}\sin\varphi_5 \\ \quad + l_6\sin\varphi_6 + l_{7-1}\sin\varphi_7 + l_8\sin(\pi + \varphi_8) = 0 \\ l_{2-2}\sin\varphi_2 + l_3\sin\varphi_3 + l_{7-2}\sin\varphi_7 \\ \quad + l_8\sin\varphi_8 + l_9\sin\varphi_9 = 0. \end{cases} \tag{9}$$

Since the number of constraint equations is three less than the number of Lagrangian coordinates, there are still

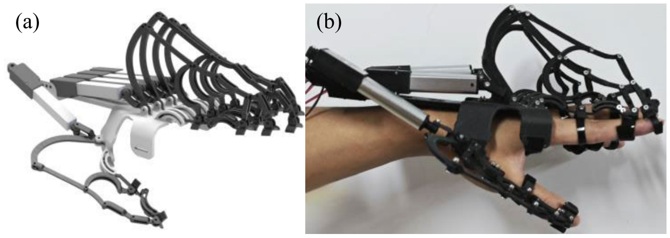


Fig. 12. 3D model of the proposed robotic glove.

three unknown Lagrangian coordinates, indicating that the mechanism has three degrees of freedom. As there is only rod $l_4$ serving as the sole driving link, the mechanism is under-actuated. In order to make the constraint equations of this mechanism solvable while also giving it human-machine fusion characteristics, we introduce the two finger joint correlation equations from the previous section into the constraint equations. Therefore, in theory, the solved exoskeleton mechanism will naturally conform to the finger's motion patterns, possess human-machine compatibility, and exert zero antagonistic pressure on the fingers.

## III. Experiment

### A. Robotic Glove Preparation and Kinematic Test

The main structural components of the robotic glove are fabricated using 3D printing technology based on a three-dimensional model, as shown in Fig. 12. The control circuit was a custom printed circuit board (PCB) with STM32F407 as the master control. A touch screen was assembled on the PCB, and an interactive program was written in the microcontroller unit (MCU). Five motor interfaces were reserved in the PCB for future development. The whole exoskeleton device was powered by a 7.4V lithium battery. TPS54302 chip was used to reduce the voltage to 3.3V for the MCU, TPS61088 boost chip was used to generate a 12V voltage for the actuator, and SLM6800 boost chip was used for charging management. The miniature linear motor was used as an actuator that integrates position and velocity feedback. The prototype system and the testing system are depicted in Fig. 13.

After assembling the prototype, the first step involved conducting a kinematic test of the robotic glove. During the testing process, the subjects kept their hands relaxed throughout and relied entirely on the robotic glove to perform 30 sets of flexion and extension movements. Simultaneously, data on the angles of the three joints were collected. The robotic glove completed one cycle of flexion and extension in 1 second, with each phase (flexion and extension) taking 400 milliseconds and a 200-millisecond pause in between. The experiment was repeated five times, with a 5-minute break between each trial. Through these experiments, angles for each joint under the exoskeleton's control were collected, and the workspace of the prototype was determined based on these angles, as shown in Fig.14.

In Fig. 14 (a), both the prototype's MCP joint end and the physiological MCP joint end exhibit a fixed trajectory and remain completely overlapped. This indicates that the equivalent rotation centers of the prototype's MCP joint and the physiological MCP joint can maintain alignment throughout the motion. In Fig. 14 (b) and (c), the prototype's PIP joint end and DIP joint end only cover the natural flexion and extension trajectory of the finger, rather than being evenly distributed throughout the physiological reachable space, as seen in typical under-actuated mechanisms. This suggests that while the robotic glove is an under-actuated mechanism, after incorporating the finger kinematic model equations, it possesses the stability of a fully-actuated mechanism, avoiding the imposition of unnatural postures on the fingers that could lead to injuries. This also highlights the kinematic advantages of the proposed novel human-machine integrated under-actuated exoskeleton structure.

To further validate whether the prototype can maintain the joint motion correlation, 20 sets of flexion angle data sequences were extracted. Based on this data, the trajectory of the prototype was generated and compared to the physiological trajectory, as shown in Fig. 15. In the figure, the prototype's motion trajectory is represented by light solid lines, while the physiological motion trajectory of the finger is represented by dark hollow dots. During the prototype experiment, each flexion phase lasted for 400 milliseconds. The figure displays trajectory points of joint ends sampled at 40-millisecond intervals, connected to represent the positions of the phalanges. The physiological phalangeal positions are depicted by light blue dashed lines, while the prototype's phalangeal positions are represented by blue solid lines. Additionally, the average trajectory point coordinates for the prototype in each posture were calculated and are denoted by red crosses.

In Fig. 15, it can be observed that during natural finger flexion and extension, the trajectory of the prototype's MCP joint end perfectly aligns with that of the finger's MCP joint end. The alignment at the PIP joint end is also extremely high. However, due to the accumulation of errors from three joint end trajectories, the alignment at the DIP joint end is lower compared to the MCP and PIP joints but still maintains a relatively high degree of overlap. The proximal and middle phalanges of both the prototype and the finger exhibit a high level of alignment. Nevertheless, there is a noticeable lag in the mid to late stages of motion, possibly due to factors such as friction and resistance, which slightly reduce the finger's movement speed when wearing the prototype. The distal phalangeal segment accumulates errors from three phalangeal segments, resulting in relatively lower alignment, especially in the later stages of flexion. However, even in this scenario, the alignment of the distal phalangeal segment remains within an acceptable range. These tests provide evidence that the proposed novel human-machine integrated under-actuated exoskeleton structure can effectively replicate the finger's kinematic model.

### B. Pressure Test of the Robotic Glove on the Finger

In order to test the static pressure, dynamic pressure, and antagonistic pressure of the novel robotic glove on the hand, we designed a multi-node pressure acquisition system, as shown in Fig. 13. The main control of the collection system uses the STM32F103C8T6 minimum system board and employs DF9-16 resistive film pressure sensors with a range of 10-500g.

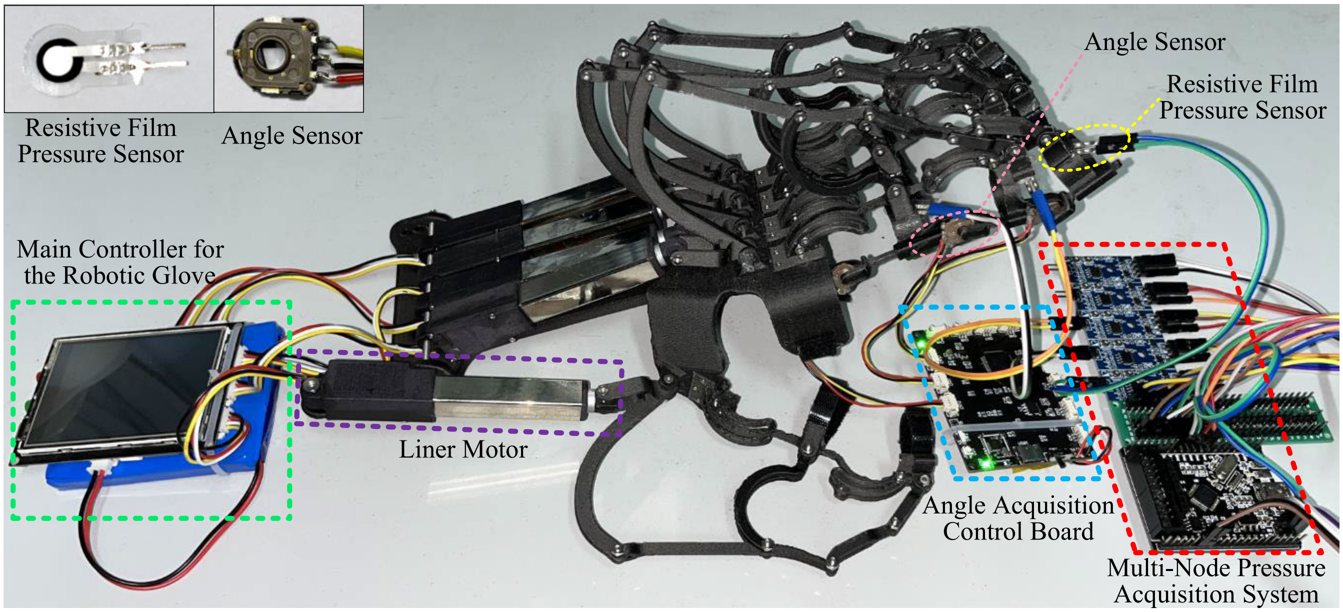


Fig. 13. The prototype and testing equipment of the proposed novel robotic glove.

TABLE I
STATIC PRESSURE AND ANTAGONISTIC PRESSURE ON EACH SEGMENT OF THE FINGER BY KINDS OF ROBOTIC GLOVES

| **Approximation** | **Pneumatic Glove** | | | **Traditional Robotic Glove** | | | **Proposed Robtic Glove** | | |
|---|---|---|---|---|---|---|---|---|---|
| | MCP | PIP | DIP | MCP | PIP | DIP | MCP | PIP | DIP |
| Static pressure (N) | 0.4 | 1.3 | 1.5 | 0.4 | 0.4 | 0.4 | 0.2 | 0.2 | 0.2 |
| Antagonistic pressure (N) | 1.3 | 1.9 | 2.3 | 1.2 | 1.1 | 0.9 | 0.7 | 0.4 | 0.3 |

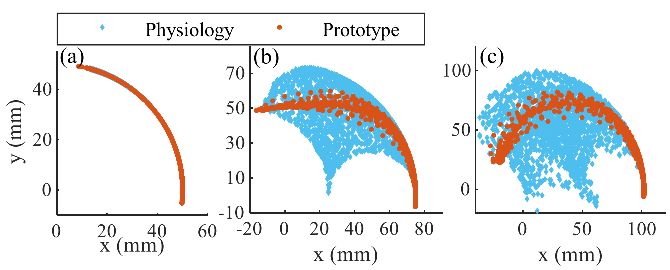


Fig. 14. Comparison of the workspace between the prototype and the physiological finger, (a) MCP joint end, (b) PIP joint end, and (c) DIP joint end.

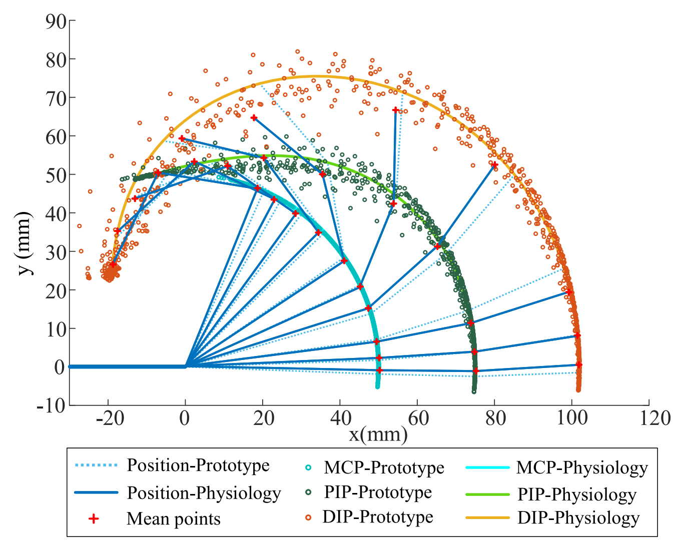


Fig. 15. Comparison of the trajectories of the joints' ends and joint motion correlations between the prototype and the physiological finger.

To emphasize the reduced pressure benefits of the novel robotic glove on the fingers, we conducted comparative experiments to assess the pressure exerted on the hand by two commonly used alternatives: pneumatic gloves [6] and linkage-type gloves [41]. For the pneumatic glove, we selected a commercially available version that operates on similar principles. The linkage-type glove was fabricated using 3D printing, following the configuration provided in [41]. We performed pressure testing at specific locations, namely the midpoints of the proximal phalanx, middle phalanx, and distal phalanx, as illustrated in Fig. 16(a). When the robotic glove was worn, pressure sensors were positioned between the fingers and the glove to enable real-time measurement of the pressure exerted by the robotic glove on each phalanx. During the pressure testing procedure, we followed these steps: initially, the robotic glove was donned, and static pressure values were recorded with the fingers in a naturally extended position. Subsequently, the robotic glove was activated to execute flexion and extension movements, and dynamic pressure values were recorded during this process. Finally, with the fingers fully flexed, resistance pressure values were recorded. This sequence was repeated for each finger, and the average pressure for each phalanx segment was calculated.

The average values of static pressure and antagonistic pressure for the three types of devices are presented in Table I. From the table, we can observe the following: (1). The pneu-

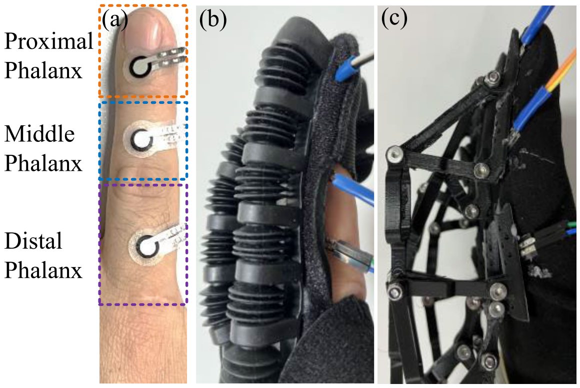


Fig. 16. Attachment positions of pressure sensors (a), and pneumatic glove (b) and traditional exoskeleton robotic glove (c) used for comparative experiments.

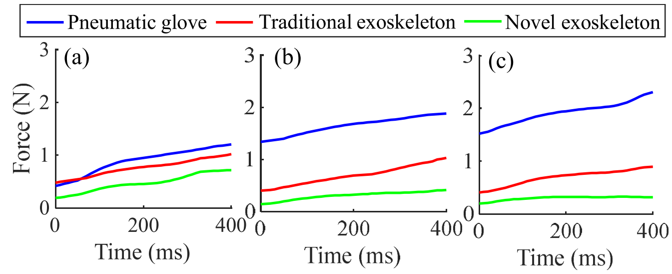


Fig. 17. Natural flexion dynamic pressure curves of (a) proximal phalanx, (b) middle phalanx, and (c) distal phalanx.

matic glove exhibits lower pressure in the proximal phalange segment but higher static pressure in the remaining segments. This is due to the pneumatic glove's fixation of the fingers starting from the middle phalanx, as depicted in Fig. 16(b). Additionally, the pneumatic glove has thicker material covering the back of the hand, and there is a deviation between the air tube deformation posture and the finger bending posture, resulting in significantly higher antagonistic pressure compared to both the traditional exoskeleton robotic glove and the novel robotic glove. (2). The traditional exoskeleton robotic glove requires applying pre-tightening force at the ring position to prevent disconnection between the exoskeleton and the fingers during motion, as shown in Fig. 16(c). Because the traditional exoskeleton robotic glove does not perfectly match the finger's kinematic model, it also exerts significant antagonistic pressure. (3). The novel robotic glove, designed to follow the natural finger motion trajectory with minimal risk of finger disconnection, requires less pre-tightening force. Experimental data shows that the novel robotic glove exerts lower antagonistic pressure compared to the other two devices. However, some antagonistic pressure remains due to the accumulation of soft tissue as the fingers are fully flexed. Table I clearly demonstrates that the proposed under-actuated robotic glove has lower static and antagonistic pressure when compared to the other two types of robotic gloves. The dynamic pressure curves of the three types of robotic gloves are shown in Fig. 17. Fig. 17(a), (b), and (c) represent the pressure curves on the proximal, middle, and distal segments of the index finger, respectively, during the flexion process for the three rehabilitation gloves. Among these, the average dynamic pressure values for these three segments of finger bones for the pneumatic glove are 0.87N, 1.63N, and 1.88N, respectively; for the traditional exoskeleton robotic glove, the average dynamic pressure values for these three segments of finger bones are 0.87N, 1.63N, and 0.66N, respectively; and for the novel robotic glove, the average dynamic pressure values for these three segments of finger bones are 0.46N, 0.34N, and 0.28N, respectively. From this, it can be observed that the novel robotic glove proposed in this study exerts significantly lower dynamic pressure on each phalange segment compared to the other two gloves. Additionally, the pneumatic glove, which is commonly considered to be more comfortable, exerts notably higher pressure on the middle and distal segments of the index finger compared to the exoskeleton-type rehabilitation glove. This difference is likely due to the significant deviation between the trajectory of finger flexion driven by the pneumatic tubing after inflation and the natural flexion trajectory of the finger. To assess the pressure applied by the proposed robotic glove on the fingers during practical use, experiments were conducted involving the grasping of everyday objects, as depicted in Fig. 18. For safety precautions, the robotic glove's drive motors were programmed to stop when the pressure sensors reached 5N to prevent any potential harm. Fig. 19(a)-(c) illustrate the pressure patterns on the proximal, middle, and distal segments of the index finger during the process of grasping a bowl. As grasping a bowl primarily involves contact with the middle and distal segments of the index finger, the pressure in the proximal segment remains below 1.2N. The maximum pressures in the middle and distal segments are 3.6N and 4.9N, respectively, both of which occur in the pneumatic glove. In contrast, the novel robotic glove registers maximum pressures of 1.6N and 3.1N in the middle and distal segments of the fingers, respectively. Fig. 19(d)-(f) display the pressure profiles on the proximal, middle, and distal segments of the index finger while grasping a water bottle. Due to the bottle's relatively narrow diameter and regular cylindrical shape, the pressure distribution on the finger segments is more uniform. The maximum pressures in the proximal, middle, and distal segments are 2.8N, 2.9N, and 4.2N, respectively, whereas the novel robotic glove registers maximum pressures of 1.6N, 1.4N, and 2.5N in the corresponding finger segments. Fig. 19(g)-(i) present the pressure patterns on the proximal, middle, and distal segments of the index finger during the process of grasping an apple. Apples, being irregularly shaped, larger in size, and relatively firm in texture, exert higher pressure on the finger segments after grasping. The maximum pressures in the proximal, middle, and distal segments are 3.0N, 4.1N, and 4.7N, respectively, while the novel robotic glove records maximum pressures of 2N, 2.5N, and 2.6N in the corresponding finger segments. From the overall analysis in Fig. 19, during real-world grasping tasks involving common objects, the novel robotic glove demonstrates superior capabilities in replicating finger movements and distributing pressure across the finger segments when compared to the pneumatic glove and the traditional exoskeleton glove. This results in reduced pressure on the finger segments, aligning with the design objectives.

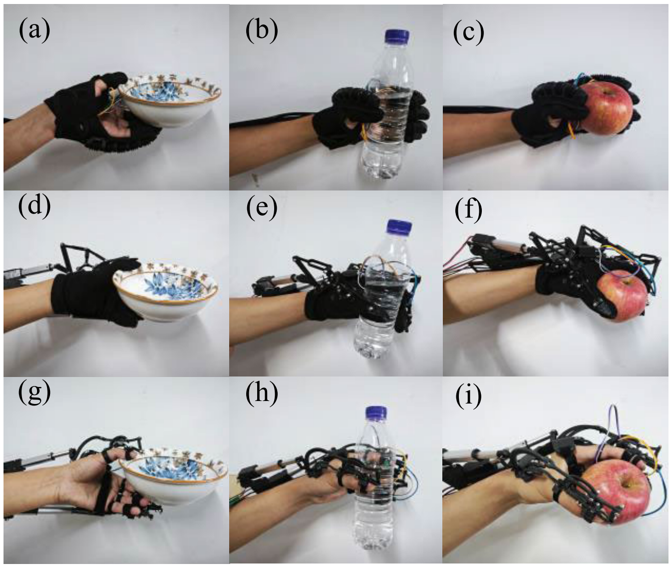


Fig. 18. Real objects grasping experiment, (a), (b), and (c) are respectively wearing the pneumatic glove to grasp the bowl, the plastic bottle, and the apple; (d), (e), and (f) are respectively wearing the traditional robotic glove to grasp the bowl, the plastic bottle, and the apple; (g), (h), and (i) are respectively wearing the proposed robotic glove to grasp the bowl, the plastic bottle, and the apple.

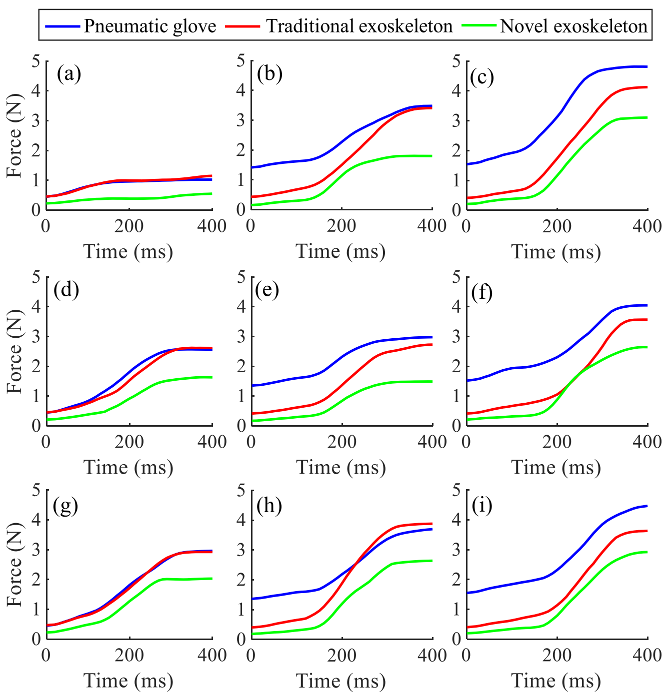


Fig. 19. Dynamic pressure curves wearing different gloves to grasp Real Objects, (a), (b), and (c) are respectively wearing the pneumatic glove to grasp the bowl, the plastic bottle, and the apple; (d), (e), and (f) are respectively wearing the traditional robotic glove to grasp the bowl, the plastic bottle, and the apple; (g), (h), and (i) are respectively wearing the proposed robotic glove to grasp the bowl, the plastic bottle, and the apple.

## IV. Conclusion

In conclusion, a robotic glove with novel under-actuated exoskeleton mechanisms is proposed in this paper. Firstly, CT images of the entire finger flexion-extension process were captured. Based on the analysis of CT data, key kinematic features of finger motion were determined, including joint CORs and equivalent rotation centers, joint rotation angle and angular velocity time-sequence functions, joint end trajectory equations, and finger joint correlations. This led to the establishment of a comprehensive and accurate finger kinematic model. Then, in the design of the novel under-actuated exoskeleton configuration, the finger kinematic model equations were introduced into the configuration constraint equations, allowing the designed under-actuated exoskeleton structure to be solvable. Theoretically, the resulting under-actuated exoskeleton configuration naturally complies with finger motion patterns. Finally, a complete prototype system and testing system were established, and both kinematic and pressure tests were conducted. In the kinematic test, the trajectories of various joint ends of the fingers after wearing the robotic glove showed a high consistency with the physiological trajectories of natural finger flexion-extension, preserving the motion correlations of each joint and simulating the natural finger motion state. Furthermore, due to the introduction of finger kinematic equations as additional constraints in the under-actuated exoskeleton structure design, the robotic glove combines the flexibility and lightness of an under-actuated structure with the stability of a fully actuated structure. In the pressure test, static pressure, dynamic pressure, and antagonistic pressure during finger flexion-extension and grasping common objects were simultaneously collected for the proposed robotic glove, a conventional pneumatic glove, and a traditional exoskeleton-structured robotic glove. The results showed that the proposed robotic glove significantly reduces the pressure on the various joints of the fingers. The device proposed in this work has great low-pressure performance, improving the comfort and safety of long-term wear for stroke patients. It has the potential to enhance the hand rehabilitation efficiency of stroke patients.

## References


[1] K. Ma, Z. Jiang, S. Gao, X. Cao, and F. Xu, "Design and analysis of fiber-reinforced soft actuators for wearable hand rehabilitation device," *IEEE Robot. Autom. Lett.*, vol. 7, no. 3, pp. 6115–6122, Jul. 2022, doi: 10.1109/LRA.2022.3167063.

[2] B. Noronha et al., "Soft, lightweight wearable robots to support the upper limb in activities of daily living: A feasibility study on chronic stroke patients," *IEEE Trans. Neural Syst. Rehabil. Eng.*, vol. 30, pp. 1401–1411, 2022, doi: 10.1109/TNSRE.2022.3175224.

[3] J. Dittli et al., "Design of a compliant, stabilizing wrist mechanism for a pediatric hand exoskeleton," in *Proc. Int. Conf. Rehabil. Robot. (ICORR)*. Rotterdam, The Netherlands: IEEE, Jul. 2022, pp. 1–6, doi: 10.1109/ICORR55369.2022.9896550.

[4] J. Iqbal and K. Baizid, "Stroke rehabilitation using exoskeleton-based robotic exercisers: Mini review," *Biomed. Res.*, vol. 26, no. 1, pp. 197–201, 2015.

[5] O. Ozioko and R. Dahiya, "Smart tactile gloves for haptic interaction, communication, and rehabilitation," *Adv. Intell. Syst.*, vol. 4, no. 2, 2022, Art. no. 2100091, doi: 10.1002.aisy.202100091.

[6] L. Cappello et al., "Assisting hand function after spinal cord injury with a fabric-based soft robotic glove," *J. Neuroeng. Rehabil.*, vol. 15, no. 1, pp. 1–10, Dec. 2018, doi: 10.1186/s12984-018-0391-x.

[7] K. Lee, P.-G. Jung, Y. Lee, and Y. Cha, "Wearable multifunctional additive hand system for enhancing the workspace and grasping capability of the human hand," *IEEE Access*, vol. 10, pp. 28094–28108, 2022, doi: 10.1109/ACCESS.2022.3157881.

[8] Y.-W. Chen, W.-C. Chiang, C.-L. Chang, S.-M. Lo, and C.-Y. Wu, "Comparative effects of EMG-driven robot-assisted therapy versus task-oriented training on motor and daily function in patients with stroke: A randomized cross-over trial," *J. Neuroeng. Rehabil.*, vol. 19, no. 1, pp. 1–9, Dec. 2022, doi: 10.1186/s12984-021-00961-w.

[9] N. Robson and G. S. Soh, "Geometric design of eight-bar wearable devices based on limb physiological contact task," *Mechanism Mach. Theory*, vol. 100, pp. 358–367, Jun. 2016, doi: 10.1016/j.mechmachtheory.2016.02.016.

[10] F. A. Nasrallah, A. Z. Mohamed, H. K. Yap, H. S. Lai, C.-H. Yeow, and J. H. Lim, "Effect of proprioceptive stimulation using a soft robotic glove on motor activation and brain connectivity in stroke survivors," *J. Neural Eng.*, vol. 18, no. 6, Dec. 2021, Art. no. 066049, doi: 10.1088/1741-2552/ac456c.

[11] C. Suulker, S. Skach, and K. Althoefer, "Soft robotic fabric actuator with elastic bands for high force and bending performance in hand exoskeletons," *IEEE Robot. Autom. Lett.*, vol. 7, no. 4, pp. 10621–10627, Oct. 2022, doi: 10.1109/LRA.2022.3194883.

[12] W. G. Darling, K. J. Cole, and G. F. Miller, "Coordination of index finger movements," *J. Biomech.*, vol. 27, no. 4, pp. 479–491, Apr. 1994, doi: 10.1016/0021-9290(94)90023-x.

[13] G. S. Rash, P. P. Belliappa, M. P. Wachowiak, N. N. Somia, and A. Gupta, "A demonstration of the validity of a 3-D video motion analysis method for measuring finger flexion and extension," *J. Biomech.*, vol. 32, no. 12, pp. 1337–1341, 1999, doi: 10.1016/S0021-9290(99)00140-2.

[14] J. Coupier, S. Hamoudi, S. Telese-Izzi, V. Feipel, M. Rooze, and S. Van Sint Jan, "A novel method for in-vivo evaluation of finger kinematics including definition of healthy motion patterns," *Clin. Biomech.*, vol. 31, pp. 47–58, Jan. 2016, doi: 10.1016/j.clinbiomech.2015.10.002.

[15] J. Yang, H. Xie, and J. Shi, "A novel motion-coupling design for a jointless tendon-driven finger exoskeleton for rehabilitation," *Mechanism Mach. Theory*, vol. 99, pp. 83–102, May 2016, doi: 10.1016/j.mechmachtheory.2015.12.010.

[16] R. Liang et al., "A general arthropod joint model and its applications in modeling human robotic joints," *IEEE Access*, vol. 9, pp. 7814–7822, 2021, doi: 10.1109/ACCESS.2021.3049469.

[17] H. Liang et al., "Barehanded music: Real-time hand interaction for virtual piano," in *Proc. 20th ACM SIGGRAPH Symp. Interact. 3D Graph. Games*, Feb. 2016, p. 8794, doi: 10.1145/2856400.2856411.

[18] F. Hess, P. Fürnstahl, L.-M. Gallo, and A. Schweizer, "3D analysis of the proximal interphalangeal joint kinematics during flexion," *Comput. Math. Methods Med.*, vol. 2013, Nov. 2013, Art. no. 138063, doi: 10.1155/2013/138063.

[19] K. N. An, E. Y. Chao, W. P. Cooney, and R. L. Linscheid, "Normative model of human hand for biomechanical analysis," *J. Biomech.*, vol. 12, no. 10, pp. 775–788, Jan. 1979, doi: 10.1016/0021-9290(79)90163-5.

[20] S. Van Sint Jan, D. J. Giurintano, D. E. Thompson, and M. Rooze, "Joint kinematics simulation from medical imaging data," *IEEE Trans. Biomed. Eng.*, vol. 44, no. 12, pp. 1175–1184, Jan. 1997, doi: 10.1109/10.649989.

[21] F. D. Kerkhof et al., "Quantifying thumb opposition kinematics using dynamic computed tomography," *J. Biomech.*, vol. 49, no. 9, pp. 1994–1999, Jun. 2016, doi: 10.1016/j.jbiomech.2016.05.008.

[22] S. Shimawaki, Y. Nakamura, M. Nakabayashi, and H. Sugimoto, "Flexion angles of finger joints in two-finger tip pinching using 3D bone models constructed from X-ray computed tomography (CT) images," *Appl. Bionics Biomech.*, vol. 2020, pp. 1–6, Sep. 2020, doi: 10.1155/2020/8883866.

[23] S. Shimawaki, T. Murai, M. Nakabayashi, and H. Sugimoto, "Measurement of flexion angle of the finger joint during cylinder gripping using a three-dimensional bone model built by X-ray computed tomography," *Appl. Bionics Biomech.*, vol. 2019, pp. 1–9, Jan. 2019, doi: 10.1155/2019/2839648.

[24] J. S. Han and H. S. Han, "Mathematical representation of articular surfaces using influence surface theory," *KSME Int. J.*, vol. 12, no. 3, pp. 380–387, May 1998, doi: 10.1007/bf02946352.

[25] T. Kataoka, H. Moritomo, J. Miyake, T. Murase, H. Yoshikawa, and K. Sugamoto, "Changes in shape and length of the collateral and accessory collateral ligaments of the metacarpophalangeal joint during flexion," *J. Bone Joint. Surg.*, vol. 93, no. 14, pp. 1318–1325, 2011, doi: 10.2106/JBJS.J.00733.

[26] P. C. Rhee, D. B. Jones, and S. Kakar, "Management of thumb metacarpophalangeal ulnar collateral ligament injuries," *J. Bone Joint Surg.*, vol. 94, no. 21, pp. 2005–2012, Nov. 2012, doi: 10.2106/jbjs.k.01024.

[27] R. Figueroa, T. J. Armstrong, C. Woolley, L. Sun, W. Zhou, and S. Sebastin, "Determining instantaneous centers of rotation for finger joints through different postures using the iterative closest point algorithm (ICP)," *Proc. Hum. Factors Ergonom. Soc. Annu. Meeting*, vol. 60, no. 1, pp. 1470–1474, Sep. 2016, doi: 10.1177/1541931213601337.

[28] X. Yang et al., "Estimation of finite finger joint centers of rotation using 3D hand skeleton motions reconstructed from CT scans," *Appl. Sci.*, vol. 10, no. 24, p. 9129, Dec. 2020, doi: 10.3390/app10249129.

[29] I. Jo, Y. Park, J. Lee, and J. Bae, "A portable and spring-guided hand exoskeleton for exercising flexion/extension of the fingers," *Mechanism Mach. Theory*, vol. 135, pp. 176–191, May 2019, doi: 10.1016/j.mechmachtheory.2019.02.004.

[30] Y. Cao, X. Yang, Z. Lim, H. Jung, D. Park, and H. You, "A linkage representation of the human hand skeletal system using CT hand scan images," *Appl. Sci.*, vol. 11, no. 13, p. 5857, Jun. 2021, doi: 10.3390/app11135857.

[31] N. Miyata, M. Kouch, M. Mochimaru, and T. Kurihara, "Finger joint kinematics from MR images," in *Proc. IEEE/RSJ Int. Conf. Intell. Robots Syst.*, Aug. 2005, Art. no. 27502755, doi: 10.1109/iros.2005.1545611.

[32] S. L. Delp, J. P. Loan, M. G. Hoy, F. E. Zajac, E. L. Topp, and J. M. Rosen, "An interactive graphics-based model of the lower extremity to study orthopaedic surgical procedures," *IEEE Trans. Biomed. Eng.*, vol. 37, no. 8, pp. 757–767, Aug. 1990, doi: 10.1109/10.102791.

[33] B. Noronha and D. Accoto, "Exoskeletal devices for hand assistance and rehabilitation: A comprehensive analysis of state-of-the-art technologies," *IEEE Trans. Med. Robot. Bionics*, vol. 3, no. 2, pp. 525–538, May 2021, doi: 10.1109/TMRB.2021.3064412.

[34] Y. Li, X. Gao, B. Liao, Y. Peng, and Y. J. Chen, "Research progress of exoskeleton for hand rehabilitation following stroke," *J. Phys., Conf. Ser.*, vol. 1820, no. 1, Mar. 2021, Art. no. 012076, doi: 10.1088/1742-6596/1820/1/012076.

[35] N. Saltybaeva, M. E. Jafari, M. Hupfer, and W. A. Kalender, "Estimates of effective dose for CT scans of the lower extremities," *Radiology*, vol. 273, no. 1, pp. 153–159, Oct. 2014, doi: 10.1148/radiol.14132903.

[36] W. Huda, K. M. Ogden, and M. R. Khorasani, "Converting dose-length product to effective dose at CT," *Radiology*, vol. 248, no. 3, pp. 995–1003, Sep. 2008, doi: 10.1148/radiol.2483071964.

[37] N. Otsu, "A threshold selection method from gray-level histograms," *IEEE Trans. Syst., Man, Cybern.*, vol. 9, no. 1, pp. 62–66, Jan. 1979, doi: 10.1109/tsmc.1979.4310076.

[38] H. Bay, A. Ess, T. Tuytelaars, and L. Van Gool, "Speeded-up robust features (SURF)," *Comput. Vis. Image Understand.*, vol. 110, no. 3, pp. 346–359, Jun. 2008, doi: 10.1016/j.cviu.2007.09.014.

[39] Y. Wu, W. Ma, M. Gong, L. Su, and L. Jiao, "A novel point-matching algorithm based on fast sample consensus for image registration," *IEEE Geosci. Remote Sens. Lett.*, vol. 12, no. 1, pp. 43–47, Jan. 2015, doi: 10.1109/LGRS.2014.2325970.

[40] L. J. Zhang, J. S. Yu, J. H. Yan, Y. H. Du, P. Xie, and Y. Q. Li, "Synthesis and optimization method of exoskeleton mechanism based on human-machine fusion," *J. Mech. Eng. Sci.*, vol. 58, no. 11, pp. 37–45, 2022, doi: 10.3901/JME.2022.11.037.

[41] I. Jo and J. Bae, "Design and control of a wearable and force-controllable hand exoskeleton system," *Mechatronics*, vol. 41, pp. 90–101, Feb. 2017, doi: 10.1016/j.mechatronics.2016.12.001.